ACADEMIC PRESS

Available online at www.sciencedirect.com

SCIENCE DIRECT®

Journal of Magnetic Resonance 159 (2002) 219–225

JMR Journal of Magnetic Resonance

www.academicpress.com

# Reciprocity and sensitivity of opposed-solenoid endovascular MRI probes

Denis Crottet,[a] Reto Meuli,[b] Stephan Wicky,[b] and Jacques J. van der Klink[a,*]

[a] *Faculté des Sciences de Base, Ecole Polytechnique Fédérale de Lausanne, CH-1015 Lausanne, Switzerland*
[b] *Diagnostic and Interventional Radiology Department, CHUV, CH-1011 Lausanne, Switzerland*

Received 17 July 2002; revised 24 September 2002

**Abstract**

Several forms of catheter-mounted "inside-out" probes for endovascular imaging have been proposed in the literature. The "opposed-solenoid" structure has been studied in relatively little detail, although it has some potential advantages over the others. Using a small water sample as a voxel, we measure point by point the spatial variation of the sensitivity and the rf field strength of such a probe, and connect the two by the reciprocity relation. By itself, the corresponding plot provides a nice example of the reciprocity relation at work; and for the characterization of the probe it gives a check on data quality. The results can be understood from simple considerations and agree well with the sensitivity observed in the image of a phantom.


*Keywords:* Endovascular imaging; Quadrupole MRI probe; Field of view

## 1. Introduction

The potential advantages of MRI receiver coil placement internal to the human body have been realized for almost as long as those of surface coils [1], but the only type in common clinical use is the endorectal coil. It is widely believed that catheter-mounted endovascular receiver probes should bring improved sensitivity for the in vivo imaging of arterial walls and (typically) atheromatous lesions, but experiments so far remain at the proof-of-principle level in animal models (dogs [2], pigs [3], rabbits [4,5], and sheep [6]). Apart from the simple solenoid probe, the main types are the twin-lead (or single-loop), the loopless, and the opposed-solenoid probes. Most experiments are performed at 1.5 T.

The twin-lead probe uses a length of short-circuited Lecher line (parallel-wire transmission line) as active element. Its length is typically 7 cm and the wire spacing 3 mm. The inflatable single-loop probe is a variant where the two wires are mounted on a balloon, so that their spacing can be adjusted in situ to the vascular diameter. A typical balloon length is 4 cm.

The active element of the loopless probe is an electric dipole. One pole is formed by a length of wire protruding from the central conductor of a coaxial cable, the other pole is distributed over the outer surface of the outer conductor of the cable. The optimum length of the single pole is slightly less than a quarter wavelength (in a medium with $\epsilon \approx 80$).

In the opposed-solenoid probe, the active element is a magnetic quadrupole, formed by a pair of coaxial solenoidal coils wound in opposite directions. The active length is determined by the gap between the coils, which is typically 6 mm or less. The coil diameter is typically 3 mm.

These different structures have fields of view of different geometry, which makes a comparison of their performance somewhat awkward. They are all ideally used with their long axis along the static magnetic field, but they remain usable to between 30° and 45° away from the optimal orientation. The opposed-solenoid and loopless probes have both a field of view with cylindrical symmetry, but the axial field of view of the loopless

* Corresponding author. Fax: +41-21-693-36-04.
*E-mail address:* jacques.vanderklink@epfl.ch (J.J. van der Klink).

1090-7807/02/$ - see front matter 
PII: S1090-7807(02)00106-4

probe is longer, which simplifies its positioning. A disadvantage of the latter type is the rather strong radial variation of sensitivity, that falls as $r^{-1}$. For a target region of annular shape (e.g., a section of the arterial wall) the opposed-solenoid provides superior homogeneity of sensitivity in comparison with several other designs [2]. At distances comparable to its wire separation the contours of constant sensitivity for a twin-lead probe are similar to ellipses, rather than circles. To optimize sensitivity, it may be advantageous to adjust the plane of the wires so as to bisect the lesion to be studied.

The sensitivity maps of the twin-lead and loopless probes have been studied in some detail both theoretically and experimentally [4,7,8]. There has been less analytical work on the opposed-solenoid probe [9] (for clinically interesting results see e.g., [5,10]), although it has three potential advantages over the other two structures. The rather constant sensitivity in an annular region has already been mentioned. Next, it is almost perfectly decoupled from the rf field of the body coil, in any position or orientation (''intrinsic decoupling'' [11]). It couples to inhomogeneities in the rf field, but not to the homogeneous part. Third, its sensitivity drops very fast at larger distances (asymptotically as $r^{-4}$), which alleviates the problem of aliasing in very high resolution imaging.

In this paper we show that simple equations can be used to optimize the dimensions of an opposed-solenoid probe for maximum sensitivity in a given annular volume outside the coils. To distinguish artifacts (effects not accounted for in the equations, such as connecting leads) from experimental errors, we measure also the spatial variation of the rf field created by the probe (even if in practical applications these probes are receive-only) and use the reciprocity relation to connect the two. There remains a single free fittable parameter that determines an overall scaling factor for the sensitivity map. That parameter can be considered a measure of the rf resistance of the coils, related to the quality factor. Incidentally the reciprocity plot, Fig. 3 below, provides a parameter-free illustration of the reciprocity relation at work, in a form that to our knowledge has not been given before. Our experiments use an opposed-solenoid probe (coils, matching and tuning capacitors) mounted on an endovascular catheter with a maximum diameter of 2 mm. A nearly identical design (except for operating frequency and coil gap) has been used recently in an ex vivo characterization of atherosclerotic plaque components [10].

## 2. Theory

In this section we first give the equations for the rf field strength that can be obtained in the space around the probe. This field strength is not important by itself, since in practice the rf pulses will be provided by the body coil of the imager, but the reciprocity relation [12] ensures that a contour of constant rf field strength is also a contour of constant detection sensitivity. The overall proportionality constant between the maps of sensitivity and of rf field contains only quantities that can be directly measured. The expression for the reciprocity relation that we use in our data analysis is given at the end of this section.

### 2.1. RF field plots

Consider a small ring of radius $a$ carrying a current $i$. At some distance, the resulting magnetic field is the same as that of a small magnetic dipole moment $m = \pi a^2 i$. Two coaxial rings, separated by $2d$ and carrying current in opposite directions, behave as a quadrupole moment $q = 2dm$. The field of a pair of small opposed solenoids is similar to that of a quadrupole. For simplicity, we restrict our considerations to a probe with its cylindrical axis parallel to the static field. (In practice, the sensitivity remains quite stable at angles up to 45° [9]). In that case, only the radial component of the field is important, and can be written as the sum of the contribution of each of the rings. Since all distances of interest will be much smaller than a wavelength, the rf magnetic field can be calculated in the zero frequency limit, starting from the standard expression for the magnetic vector potential for a stationary current density, see e.g., [13]. The result is

$$B_{\mathrm{r}}(r,\phi,z) = B_{\mathrm{r}}^{(+)}(r,\phi,z) + B_{\mathrm{r}}^{(-)}(r,\phi,z), \tag{1a}$$

$$B_{\mathrm{r}}^{(\pm)}(r,\phi,z) = -\frac{\mu_0}{4\pi}\frac{i}{a}\frac{d\pm z}{a}\left(\frac{ap_\pm}{r}\right)^{3/2} \times \frac{1}{2p_\pm}\left(\frac{2+p_\pm}{1+p_\pm}E(-p_\pm) - 2K(-p_\pm)\right), \tag{1b}$$

$$p_\pm(r,z) = \frac{4ra}{(r-a)^2 + (d\pm z)^2}, \tag{1c}$$

where $K(p)$ and $E(p)$ are the elliptic integrals of the first and second kind. For a structure with more than one turn on each of the two coils, the field is calculated by summing Eq. (1a) over a corresponding number of pairs at increasing $d$. The lines drawn in Figs. 1, 2 and 4 below have all been calculated from Eqs. (1a)–(1c) with a loop radius $a = 0.9$ mm. This corresponds to the center of the 0.2 mm diameter wire used to wind coils with an outer diameter of 2 mm. The separation of the loops was set to 0.22 mm and the gap to 8 mm. (More data on probe construction are given in the experimental section.) According to the reciprocity relation, Eq. (4a) below, the plot of $B_{\mathrm{r}}/i$ as function of position $(r,\phi,z)$ has the same shape as the plot of signal to noise ratio ($S/N$) as a function of position. The geometry that we discuss here

has cylindrical symmetry, and, therefore, $\phi$ does not appear on the right-hand side of Eqs. (1a)–(1c).

Contours of constant $B_r/i$ are shown in Fig. 1. By symmetry, the radial field $B_r$ (and, therefore, also the sensitivity) is zero on the $z$-axis. Furthermore, there are two surfaces (nearly straight lines on the figure) where the contributions from the the top and bottom coils cancel, resulting in zero sensitivity. The interesting volume for the use of the structure as a probe is in between these surfaces, because the contours reach out relatively far along the $r$-axis. The radial variation of the sensitivity in the $z = 0$ plane is shown in Fig. 2a. The maximum in Fig. 2a actually represents a saddlepoint in the $(r, z)$ plane, as can be seen from the crossing of the two contours of value 1 on Fig. 1. The absolute maxima of the sensitivity fall outside the $z = 0$ plane (at the centers of the two half-circle contours marked "2" in Fig. 1), but the sensitivity changes rapidly in their neighborhood, so that these regions are not particularly interesting for imaging. One of them appears near $z = 3.8$ mm in Fig. 2b, that shows the variation of sensitivity on the (upper-half) plane $r = 2$ mm. The extremum near $z = 10$ mm in that figure is again in a region of rapidly varying sensitivity. It is not suitable for imaging, but can be used for localizing the coils in a scout image. The most useful region for imaging is the annulus from $r \approx 2$ onwards on Fig. 2a and of a thickness comparable to the gap, as shown in Fig. 1.

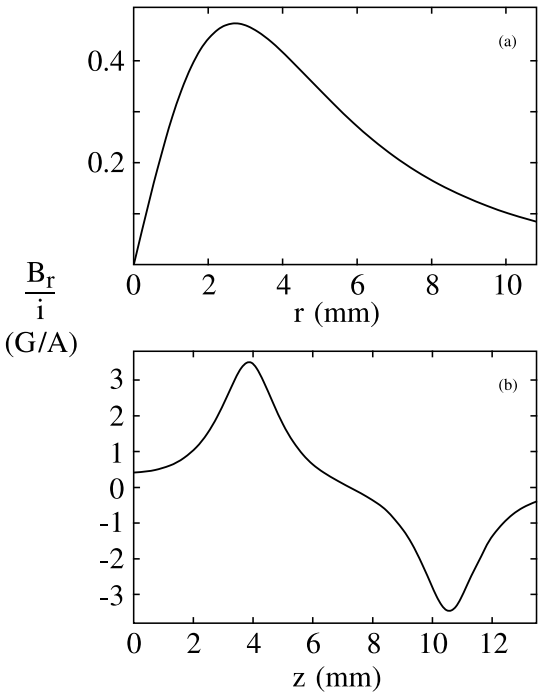


Fig. 2. Sensitivity curves for the same structure as in Fig. 1, in the same coordinate system. (a) Variation along $r$ in the $z = 0$ plane. The maximum corresponds to the crossing point of the two contours of value 1 on Fig. 1. (b) Variation along $z$ on the surface of radius 2 mm.

### 2.2. Reciprocity equations

The solution of Larmor's equation for the motion of a magnetic moment $\mathbf{m}$ in a static field $\mathbf{B}_0$ is, for positive $\gamma$, a left-handed (indicated by a subscript $-$) precession of $\mathbf{m}$ around $\mathbf{B}_0$. In phasor notation, where $\mathsf{m}(\mathbf{r})$ is the phasor corresponding to the vector $\mathbf{m}(\mathbf{r}, t)$, the magnetic moment of a voxel at $\mathbf{r}$, and with the external field along $z$

$$\mathsf{m}(\mathbf{r}) = \mathsf{m}_-(\mathbf{r}) = m_-(\mathbf{r}) \exp(-\mathrm{i}\varphi_m(\mathbf{r}))(\hat{\mathbf{x}} - \mathrm{i}\hat{\mathbf{y}}), \tag{2}$$

where $m_-$ is the magnitude of the transverse magnetic moment and $\hat{\mathbf{x}}$ a unit vector. A general ellipsoidally polarized transverse rf magnetic field phasor can be written as a superposition of a right-handed (subscript +) and a left-handed (subscript $-$) phasor

$$\mathsf{B}_\pm(\mathbf{r}) = B_\pm(\mathbf{r}) \exp(-\mathrm{i}\varphi_\pm(\mathbf{r}))(\hat{\mathbf{x}} \pm \mathrm{i}\hat{\mathbf{y}}) \tag{3}$$

and $\varphi_m(\mathbf{r}) = \varphi_-(\mathbf{r}) - \pi/2$, because in every point $\mathbf{r}$ the rotating magnetic moment $\mathbf{m}_-$ is in quadrature with $\mathbf{B}_-$. The difference $\varphi_+(\mathbf{r}) - \varphi_-(\mathbf{r})$ describes an $\mathbf{r}$-dependent orientation of the rf field (as exists in the opposed-solenoid and most other inside-out probes); the sum $\varphi_+(\mathbf{r}) + \varphi_-(\mathbf{r})$ describes retardation effects.

Let $i\cos(\omega t)$ be the current injected into the probe connector (*not* the coils) during transmission, and $V(\mathbf{r})\cos(\omega t + \varphi_V(\mathbf{r}))$ the signal voltage appearing on that connector due to $\mathbf{m}(\mathbf{r}, t)$. With those notations, the reciprocity relation is given by the pair of real equations

$$iV = 2\omega B_+ m_-, \tag{4a}$$

$$\varphi_V(\mathbf{r}) = \varphi_+(\mathbf{r}) + \varphi_-(\mathbf{r}) - \pi/2. \tag{4b}$$

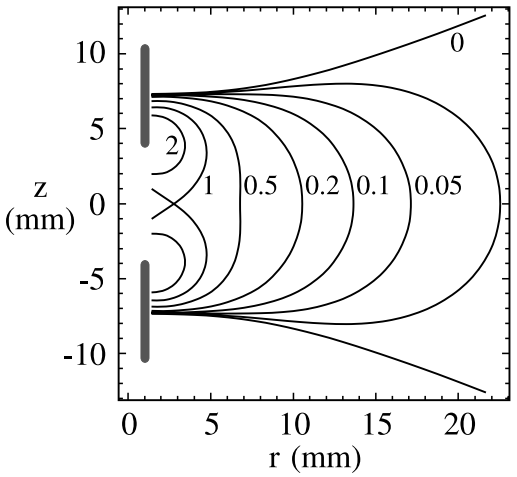


Fig. 1. Contours of constant radial magnetic field $B_r$ are drawn on the $(r, z)$ plane for an opposed-solenoid structure with 30 turns per coil, and a coil separation of 8 mm. The position of the windings is indicated by the grey bars. The contours are labeled in terms of relative amplitude of $B_r$, where the maximum value in the $z = 0$ plane has been set to 1. The full 3D picture is obtained by rotating the figure around the $z$-axis. The interesting region for magnetic resonance is in between the two lines $B_r = 0$ (top and bottom contours).

If there are no retardation effects, the $\varphi_+ + \varphi_-$ are **r**-independent and the signals $V(\mathbf{r})$ from voxels at different **r** add coherently. This will be the usual case for intravascular MRI.

For the determination of the time domain ratio of signal voltage to rms-noise voltage $(S/N)_t$ we suppose that, looking into the connector at resonance, the impedance $R$ of the probe is real. The Johnson noise voltage generated by the probe in a bandwidth $\Delta\nu$ has rms amplitude $n_{\rm rms} = 2(kTR\Delta\nu)^{1/2}$. The power injected by the transmitter to create the rotating rf field $\mathbf{B}_+(t)$ is $P = \frac{1}{2}Ri^2$. We can calibrate $\mathbf{B}_-(t)$ (but, in the general case, *not* $\mathbf{B}_+(t)$) from the length $\tau_{\pi/2}$ of the $\pi/2$ pulse. In the following we assume the usual situation where $B_+$ in Eq. (4a) is equal to $B_-$. Let $m_- = \mathscr{M}$, the equilibrium nuclear magnetic moment of the voxel. Assuming a perfect rectangular filter of width $\Delta\nu$, we have from the usual definition of $(S/N)_t$

$$(S/N)_t \equiv \frac{V}{2\sqrt{kTR\Delta\nu}} = \frac{\omega B_-\mathscr{M}}{\sqrt{2kT\Delta\nu P}} = \frac{\pi}{2\sqrt{\Delta\nu}}\frac{\mathscr{M}B_0}{\sqrt{2kTP}}\frac{1}{\tau_{\pi/2}}. \quad (5)$$

The signal to noise ratio in the frequency domain spectrum $(S/N)_{\rm f}$ is defined as the amplitude of the absorption peak, divided by the rms noise in the absorption spectrum. For a simple exponential sampled at $N_{\rm f}$ points with dwell time $1/\Delta\nu$

$$(S/N)_{\rm f} = \frac{T_2^*\Delta\nu}{\sqrt{N_{\rm f}}}(S/N)_t = \frac{\pi T_2^*\sqrt{\Delta\nu}}{2\sqrt{N_{\rm f}}}\frac{\mathscr{M}B_0}{\sqrt{2PkT}}\frac{1}{\tau_{\pi/2}}. \quad (6)$$

This equation will be used to analyze the experimental data in Fig. 3 below. For a simple spin–echo imaging sequence, where $M_i$ phase-encoded traces are acquired, each consisting of $N_i$ points sampled at a dwell time $1/\Delta\nu$, the ratio of voxel signal amplitude to rms noise is

$$(S/N)_i = \sqrt{N_iM_i}(S/N)_t \quad (7)$$

and this equation will serve to connect the results obtained using the probe in an actual imaging sequence, Fig. 6 below, to those from small-sample spectroscopic experiments, Fig. 4c below.

As a side remark we note that these reciprocity relations also hold for the loopless probe [7], although this is not evident from proofs based upon Faraday's law [12], that perform an integration over a closed loop. A proof based on Poynting's theorem covers all types of probe [14].

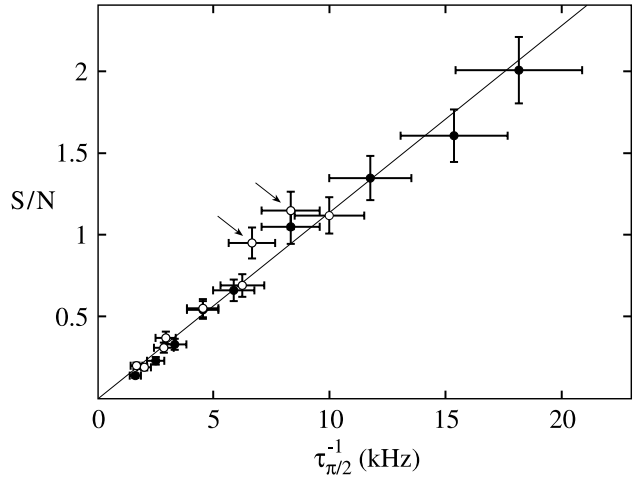


Fig. 3. Experimental relation between spectral signal-to-noise ratio $(S/N)_{\rm f}$ and inverse of the $\pi/2$-pulse length $\tau^{-1}_{\pi/2}$. The parameter of the points is the position $(r,z)$ of the 0.54 μl water sample with respect to the center of the opposed solenoids, the axes system of Fig. 1. Open circles measured at $z = 0$ mm, filled circles at $z = 2$ mm.

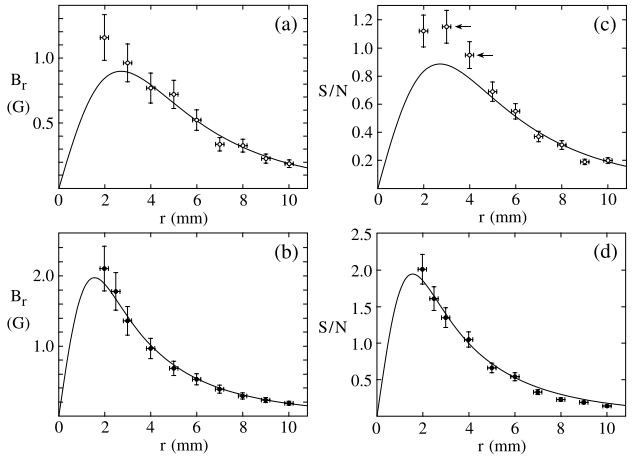


Fig. 4. In this figure the same field strength and sensitivity data as in Fig. 3 are plotted explicitly as function of position of the small water sample in the axes system of Fig. 1. Panels (a) and (c) are taken in the plane $z = 0$, panels (b) and (d) in the plane $z = 2$ mm. The full curves in (a) and (c) have the same shape as Fig. 2a. In principle, just one single fittable constant (the ratio of the vertical scales in panel (a) and in Fig. 2a) connects all four panels to the theoretical results of Eqs. (1a)–(1c) and (6).

## 3. Experimental

Our catheter probes are from the same supplier (see Acknowledgments) as those used in [10]. The resonant frequencies, the number of turns per coil, and the gap length were adapted to our specifications. The electronic circuits and the catheter dimensions are the same. The coils on our probes have 30 turns each, extending over a 6.5 mm length, and the gap is 8 mm. The wire diameter is 0.2 mm. The outer diameter of the coils is 2 mm, and the inner diameter of the coil form is compatible with that of one lumen of the 70 cm long 5F dual-lumen catheter on which it is mounted. Tuning and matching is performed with two miniature capacitor chips, imbedded in the other lumen near the coil, in a standard serial-tuned, parallel-matched configuration. That same lumen also

contains the miniature coaxial cable that connects the probe to the spectrometer electronics. The resonance frequency corresponds to a 1.5 T field. The capacitors can be very small (with low voltage ratings) since under imaging conditions the transmit-only body coil is intrinsically decoupled from the receive-only catheter probe.

The tuning and matching elements are adjusted with the coils in saline solution, and a typical $Q$ value measured on a Hewlett Packard 8712ET network analyzer is about 40. Changing from saline solution to air mainly affects the resonance frequency, that increases by several MHz, while the $Q$ does not change significantly. There are no notable changes in $Q$ or resonance frequency when the saline solution is replaced with tap water. These results show that the rf resistance of the probe is to a large extent be determined by the coil itself, rather than by the ambient loading.

A first series of experiments was performed on a simple NMR spectrometer. A catheter probe was used in both (low-power) transmit and receive modes. A small glass capillary (0.9 mm dia) was filled over a length of 0.85 mm with water doped with $CuSO_4$ (4.64 g/L). A mechanism was built to vary precisely the distance between the opposed-solenoid and this sample in both the radial and axial directions. For each distance, the length of the $\pi/2$ rf pulse was determined, and the signal-to-noise ratio in the spectrum was measured. While it is possible to obtain a full $(S/N)$ map from a single image taken in a large volume of water, it is not possible to obtain a $B_r/i$ map that way: hence the need for a point by point method using a small water sample and with the catheter in air. The resulting misadjustment of the electronic resonance frequency of the probe was compensated by an increase in magnetic field, and the change in probe impedance was only slight, judging from the reflected transmitter power.

In a second experiment, an image of a phantom was made on a Siemens Symphony machine, using the body coil in transmit and the catheter probe in receive mode. We image the water-filled holes in a Teflon cylinder, 20 mm dia by 8 mm height. In its centerplane are 3 diametral holes of 0.8 mm dia. They are used to align the imaging plane with the $z = 0$ plane of the opposed-solenoid. Parallel to the axis is one hole in the center of 2 mm dia (the catheter coil is centered in this hole) plus six series of holes of 0.7 mm dia. There are also three semicircular cutouts along the outer cylinder surface. The phantom fits rather snugly inside a glass tube filled with water doped with $CuSO_4$ at the same concentration as before. As observed on the circuit analyzer, the resonance frequency of the probe is now very close to the operating frequency of the imager. The data matrix is $512 \times 256$, the filter width $\pm 16$ kHz, and the voxel volume $0.2 \times 0.2 \times 2\,\text{mm}^3$. The sequence is spin echo, with an echo time of 20 ms. The doped water has $T_2 = 50$ ms, so the doping attenuates the signal by $\exp(-20/50) \approx 0.67$. The number of scans was four.

## 4. Results

We have measured two lines in the sensitivity and rf field maps using the NMR spectrometer and the small water sample, one at $z = 0$, the other at $z = 2$ mm. In both cases the radial distance was varied between 2 and 10 mm. There are 19 datapoints all together, each consisting of a determination of the single-scan signal-to-noise ratio in the frequency domain, $(S/N)_f$, and of the inverse of the length of the $\pi/2$-pulse, $\tau_{\pi/2}^{-1}$. They are shown in Fig. 3. The slope of the linear regression line is 114 μs, while the calculated value using Eq. (6) is 123 μs ($\mathscr{M} = 2.6325 \times 10^{-12}\,\text{A m}^2$; $B_0 = 1.5$ T; $P = 64$ W (calculated from the transmitter output into a 50 Ω load, as observed on an oscilloscope); $N_f = 1024$; $\Delta\nu = 5$ kHz; $kT \approx 4 \times 10^{-21}$ J; $T_2^* = 6.4$ ms). The agreement is very satisfactory, although it is likely that there are some compensating errors in the measured parameters: the actually measured $(S/N)$ should be less than the quantity appearing in the equation (because of the additional noise produced by the preamplifier) while the actually measured $P$ should be larger than the quantity in the equation (because of anharmonicity and of network losses). There are two experimental points (indicated by arrows on Fig. 3) that lie rather far outside the regression line, which suggest some measurement error other than a faulty determination of $(r, z)$. We come back to these below.

Next we consider the two individual plots of rf field strength as a function of distance in Figs. 4a and b, and compare them with the calculated curves of $B/i$ in Fig. 2. From the length of the $\pi/2$ pulse the experimental value of $B$ can be deduced, but there is no simple way to measure the experimental $i$, and, therefore, the current $i_{\text{pulse}}$ that runs through the coils during the pulse is a fittable constant. A satisfactory fit of the data in Figs. 4a and b can be obtained by setting $i_{\text{pulse}} = 1.91$ A. Note that this $i_{\text{pulse}}$ is not the same quantity as the $i$ appearing in Eq. (4a). The former is the rf current in the wire of the coil, the latter is the current flowing into the "connector" of the probe. The two are related by an impedance transformation inside the probe, the details of which we do not need to know.

With 64 W dissipated in the probe, and assuming 2–3 dB loss in the thin coaxial cable, the rf resistance of the coils is found as 17–22 Ω. The 0.2 mm diameter copper wire used to wind the coils is about 37 cm long. The rf resistance of a straight wire of that length is ≈1.2 Ω. However, in this closely wound structure of two heavily coupled solenoids the proximity effect reduces the section of the wire available to the rf current much below that in a straight wire. While a value of 15–20 for

this reduction does not seem unreasonable (even for an optimally wound single solenoid it will be around 3 [12]), it would be difficult to calculate. The resistance measured in air does not increase much further in water or in saline solution, as has been found from $Q$ determinations.

Combining the fits in the reciprocity plot, Fig. 3, and in the rf field strength plots, Figs. 4a and b, we obtain the curves for the signal-to-noise ratio in Figs. 4c and d. The points indicated by an arrow in Fig. 4c are the same as those in Fig. 3, which suggests an error in the $(S/N)$ measurements. For $r \approx 2\,\text{mm}$, the values are off the theoretical curve in both Figs. 4a and c, but their ratio satisfies the reciprocity condition. Here the reason seems to be that part of the finite-length sample is outside the $z = 0$ plane, where the sensitivity (for small $r$) is larger, compare Fig. 2b.

The curve in Fig. 4c can be used with Eqs. (6) and (7) to predict the expected signal to noise ratio under imaging conditions. The phantom image is given in Fig. 5, where the midplane of the probe ($z = 0$ in the equations) coincides with the midplane of the phantom. In principle all holes are filled with water, but it is seen that the filling is not perfect (the choice of Teflon as a material is not optimal in this respect). The narrow annular region between the Teflon cylinder and the inner wall of the water-filled glass tube can be seen on the image. One of the diametral holes (at "seven o'clock") has not filled completely with water. The second axial hole at two o'clock probably has a small air bubble. The first hole at four o'clock has high intensity: this is an artifact associated with the return wire from the end of the outer coil

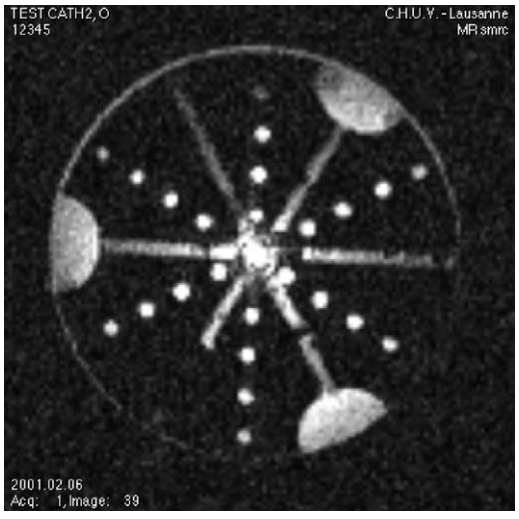


Fig. 5. Image of a polymer cylinder (dark circle) with water-filled holes (light circles, half-circles, and lines) in it. The outer circle has 20 mm diameter. In the axes system connected to the opposed-solenoid probe, Fig. 1, this is the $z = 0$ plane. The center of the image corresponds to $r = 0$. The radial variation in intensity of the bright spots can be seen more clearly in Fig. 6.

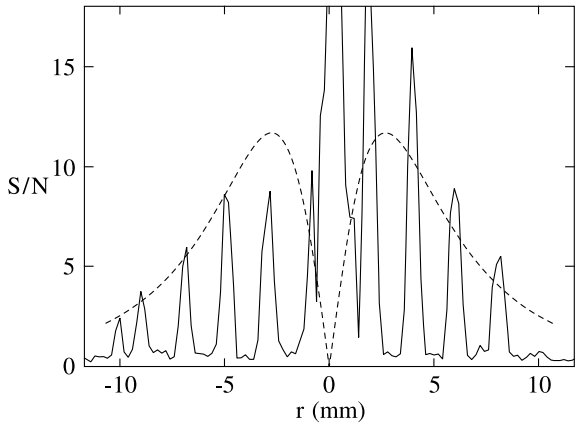


Fig. 6. Experimental data for signal to noise ratio along a line of holes in the image of Fig. 5. The dashed curve is the value expected from Fig. 4c.

on the catheter back to the coaxial cable and/or the wire connecting the two coils.

The signal to noise ratio in Fig. 5, scaled to a single scan, along a line crossing the series of axial holes from ten o'clock to four o'clock is shown in Fig. 6. The rms noise in a phase spectrum equals the average amplitude in the black areas of a magnitude image like Fig. 5. The four o'clock branch in Fig. 6 has an artificial high intensity, as already seen qualitatively on the image. The data for the ten o'clock branch correspond reasonably well with the dashed curve, predicted from Fig. 4c. If undoped water is used to obtain the image, $(S/N)$ is 50% higher, because of relaxation effects during the echo time in the imaging sequence. The visualization software used to extract Fig. 6 from the image Fig. 5 provides no way to ensure that such a line of data passes through the center of the image of every hole in the phantom, and a deviation such as near $r = -3\,\text{mm}$ in Fig. 6 could be due to the pixel being on the edge, representing partially the zero intensity outside the hole.

## 5. Discussion

The calculation represented in Fig. 2 gives a good understanding of Fig. 6. Therefore, Eq. (1a) can be used to pick the quadrupole geometry most suited to obtain a desired field of view in endoluminal imaging with an opposed-solenoid probe. The most crucial parameter is the gap length. Compared to the twin-lead and loopless probes, the opposed-solenoid has a short axial field of view, and increasing it comes at a big price in $(S/N)$: if the gap of our probe could be halved while keeping all other things equal, the sensitivity would increase by a factor of four. In the ex vivo application of [10], the small gap chosen there (2 mm) probably does not complicate the correct positioning of the probe and yields an important advantage in $(S/N)$, but such short fields of

view may be of limited use in vivo, with the coils sitting at the end of 70 cm or so of catheter.

The rather high rf resistance of our coils suggests that some improvement in $(S/N)$ can be obtained by diminishing the number of turns. From calculations as for Fig. 2 it is found that halving their number requires an increase of 20% in $i_{\text{pulse}}$ to maintain the same $B_{\text{r}}$. If the rf resistance is proportional to the number of turns the required power $P$ drops by 28%, and according to Eq. (6) the sensitivity should increase by 18%. This result is specific to the quadrupole character of the probe: for a solenoid (a magnetic dipole) the sensitivity is independent of the number of turns, see e.g., [15].

Bearing in mind these considerations, as well as the geometry differences between the intravascular probe types mentioned in the introduction, we make some rough comparisons between the (few) published sensitivity maps. In the imaging experiment, the probe presented here has for a 0.08 μl voxel of undoped water and the imaging parameters given in the experimental section a single-scan $(S/N) \approx 18$ on an annulus of a few mm wide, 8 mm high, and 6 mm diameter. This corresponds to $(S/N) \approx 65$ under the imaging conditions of Figs. 5c and d in [8] for two different expandable single-loop probes, or $(S/N) \approx 13$ under the conditions of Fig. 6b in [4] for a twin-lead probe or Fig. 11 in [7] for a loopless probe. The corresponding experimental results coincide within a factor of two or so, which is perhaps not astonishing given that all probes have been developed for application within vessels of typically that 6 mm diameter.

Another question is what actually can be gained with respect to the use of a surface coil, which has the advantage of not requiring an endovascular intervention. Such comparisons have been made [5,9] for a typical 13 cm surface coil. At a depth below the surface at which such a surface coil is optimal, the opposed-solenoid used in [9] (with a gap comparable to that used here) had in its optimum annulus an order of magnitude better sensitivity. The authors of [5] use the surface coil at a larger distance, which makes the comparison a bit unfair; but they present also relative rankings for an opposed-solenoid, a twin-lead and a loopless probe that they constructed. As in our comparison with [8], they find their opposed-solenoid and twin-lead probes similar in performance. Rather amazingly, their loopless probe performed very poorly, perhaps because the pole length was short compared to what should be [7] the optimum value.

Including the present work, theoretical and experimental data are available for the sensitivity maps of opposed-solenoid, twin-lead [4,8], and loopless [7] probes. When the designs are optimized towards a short, narrow target region, and the probes are optimally placed, their $(S/N)$ performances can be rather comparable. The opposed-solenoid has the best radial homogeneity, but the two other designs have a longer axial field of view. Endovascular coils can provide an interesting gain in $(S/N)$ with respect to surface coils for vasculature at more than a few centimeters below the skin [5,9].

## Acknowledgments

This work has been supported by the Fund for Common Research UNIL-EPFL. We thank Eelke Visser, Wilfred Heiner and Yvonne Hoogeveen at Cordis Europa (Roden, the Netherlands) for providing the catheter probes and for illuminating discussions.

## References

[1] G.C. Hurst, G.J. Misic, in: D.M. Grant, R.K. Harris (Eds.), Encycl. Magn. Res., Wiley, New York, 1996, pp. 1373–1378.
[2] G.C. Hurst, J. Hua, J.L. Duerk, A.M. Cohen, Magn. Reson. Med. 24 (1992) 343.
[3] A.J. Martin, R.M. Henkelman, Magn. Reson. Med. 32 (1994) 224.
[4] E. Atalar, P.A. Bottomley, O. Ocali, L.C.L. Correia, M.D. Kelemen, J.A.C. Lima, E.A. Zerhouni, Magn. Reson. Med. 36 (1996) 596.
[5] P.A. Rivas, K.S. Nayak, G.C. Scott, M.V. McConnell, A.B. Kerr, D.G. Nishimura, J.M. Pauly, B.S. Hu, J. Cardiovasc. Magn. Reson. 4 (2002) 223–232.
[6] H.H. Quick, M.E. Ladd, D. Nanz, K.P. Mikolajczyk, J.F. Debatin, Magn. Reson. Med. 42 (1999) 738.
[7] O. Ocali, E. Atalar, Magn. Reson. Med. 37 (1997) 112.
[8] H.H. Quick, M.E. Ladd, G.G. Zimmerman-Paul, P. Erhart, E. Hofmann, G.K. von Schulthess, J.F. Debatin, Magn. Reson. Med. 41 (1999) 751.
[9] A.J. Martin, D.B. Plewes, R.M. Henkelman, J. Magn. Reson. Imaging 2 (1992) 421–429.
[10] W.J. Rogers, J.W. Prichard, Y.L. Hu, P.R. Olson, D.H. Benckart, C.M. Kramer, D.A. Vido, N. Reichek, Arterioscler. Thromb. Vasc. Biol. 20 (2000) 1824–1830.
[11] J.S. Hyde, in: D.M. Grant, R.K. Harris (Eds.), Encycl. Magn. Res., Wiley, New York, 1996, pp. 4656–4664.
[12] D.I. Hoult, R.E. Richards, J. Magn. Reson. 24 (1976) 71.
[13] R.K. Cooper, J.A. Jackson, J. Magn. Reson. 41 (1980) 400.
[14] J.J. van der Klink, J. Magn. Reson. 148 (2001) 147.
[15] U. Haeberlen, Bull. Ampere 45 (2/3) (1996) 13.